van den Bosch Aletta Marthe Roswitha (Orcid ID: 0000-0001-8886-8928)

Ultrastructural axon-myelin unit alterations in MS correlate with inflammation

Aletta M.R. van den Bosch[1], Sophie Hümmert[2], Anna Steyer[2], Torben Ruhwedel[2], Jörg Hamann[1,3], Joost Smolders[1,4], Klaus-Armin Nave[2], Christine Stadelmann[5], Maarten H. P. Kole[6,7], Wiebke Möbius[2*], Inge Huitinga[1,8*]

[1]Department of Neuroimmunology, Netherlands Institute for Neuroscience, Royal Netherlands Academy for Arts and Sciences, Amsterdam, The Netherlands

[2]Department of Neurogenetics, Max Planck Institute for Multidisciplinary Sciences, Göttingen, Germany

[3]Department of Experimental Immunology, Amsterdam institute for Infection and Immunity, Amsterdam UMC, Amsterdam, The Netherlands

[4]Department of Neurology and Immunology, MS center ErasMS, ErasmusMC, Rotterdam, The Netherlands

[5]Department of Neuropathology, University Medical Center Göttingen, Göttingen, Germany

[6]Department of Axonal Signaling, Netherlands Institute for Neuroscience, Royal Netherlands Academy for Arts and Sciences, Amsterdam, The Netherlands

[7]Cell Biology, Neurobiology and Biophysics, Department of Biology, Faculty of Science, University of Utrecht, Utrecht, The Netherlands

[8]Swammerdam Institute for Life Sciences, University of Amsterdam, Amsterdam, The Netherlands

[*]authors contributed equally

Keywords: transmission electron microscopy/multiple sclerosis/axon-myelin unit

Manuscript length: 21 pages (250 words in abstract; 1457 words in discussion; 4687 words in main text), 2 tables, 6 figures, 45 references

Corresponding author: Aletta van den Bosch or Inge Huitinga, Neuroimmunology Research Group, Netherlands Institute for Neuroscience, Meibergdreef 47, 1105 BA Amsterdam The Netherlands, a.v.d.bosch@nin.knaw.nl or i.huitinga@nin.knaw.nl

This article has been accepted for publication and undergone full peer review but has not been through the copyediting, typesetting, pagination and proofreading process which may lead to differences between this version and the Version of Record. Please cite this article as doi: 10.1002/ana.26585

Summary for social media if published

Twitter handle: @aletta_vdbosch

Previous studies show loss of myelin stability in the normal appearing white matter (NAWM) of multiple sclerosis (MS). In this study we systematically quantified ultrastructural characteristics of the axon-myelin unit in NAWM of MS and control brain tissue at the subcellular level and correlated it to local neuro-inflammation. We show that in NAWM in MS the nodes of Ranvier are disorganized, the myelin is less compact and there is an increase of axonal mitochondria, correlating to activated microglia and correlates with increased neuro-inflammation. These changes in de NAWM of MS may contribute to disease progression and predispose the tissue for lesion formation.

Abstract

Objective: Changes in the normal-appearing white matter (NAWM) in multiple sclerosis (MS) may contribute to disease progression. Here, we systematically quantified ultrastructural and subcellular characteristics of the axon-myelin unit in MS NAWM and determined how this correlates with low grade inflammation.

Methods: Human brain tissue obtained with short post-mortem delay and fixation at autopsy enables systematic quantification of ultrastructural characteristics. In this study, we performed high-resolution immunohistochemistry and quantitative transmission electron microscopy to study inflammation and ultrastructural characteristics of the axon-myelin unit in MS NAWM (n=8) and control white matter (WM) in the optic nerve.

Results: In the MS NAWM, there were more activated and phagocytic microglia cells ($HLA^+P2RY12^-$ and $Iba1^+CD68^+$) and more T cells ($CD3^+$) compared to control WM, mainly located in the perivascular space. In MS NAWM compared to control WM there were, as expected, longer paranodes and juxtaparanodes and larger overlap between paranodes and juxtaparanodes. There was less compact myelin wrapping, a lower g-ratio, and a higher frequency of axonal mitochondria. Changes in myelin and axonal mitochondrial frequency correlated positively with the number of active and phagocytic microglia and lymphocytes in the optic nerve.

Interpretation: These data suggest that in MS NAWM myelin detachment and uncompact myelin wrapping occurs, potassium channels are unmasked at the nodes of Ranvier, and axonal energy demand is increased, or mitochondrial transport is stagnated, accompanied by increased presence of activated and phagocytic microglia and T cells. These sub-clinical alterations to the axon-myelin unit in MS NAWM may be contributing to disease progression.

Introduction

Multiple sclerosis (MS) is a chronic inflammatory disease of the central nervous system (CNS), with focal demyelinated lesions throughout [19, 22]. In early as well as advanced progressive MS, lesions arise from the normal-appearing white matter (NAWM) and there is substantial inflammatory activity. Compared to control white matter, in MS, the NAWM is affected by astrogliosis, axonal loss, increased oxidized phospholipids, lesion-like microglial activation, and reorganization of the paranodes and juxtaparanodal domains [2, 3, 11, 13, 24, 30].

Little yet is known about the axons and myelin at the subcellular level in NAWM in MS and how these correlate with inflammation. The myelin sheath, characterized by a multilamellar structure of multiple lipid-rich plasma membranes surrounding the axons, enables rapid impulse propagation, known as saltatory conduction [7]. In the CNS, myelin sheaths are formed by oligodendrocytes wrapping and compacting multiple layers of membranes around the axon that become flanked by nodes of Ranvier. Myelin thickness is typically correlated to the axon caliber [9]. In between the axon and the innermost myelin layer lies the inner tongue, where myelin membrane incorporation occurs [26, 37], and the extracellular peri-axonal space, which together with the myelinic channels is important for axonal metabolic support [7, 29]. These areas, which are possibly critical to MS pathology, are only visible at the ultrastructural level.

In experimental animal models for MS, detachment of myelin from the axon occurs in the NAWM and this increases over time [4], and by biochemically altering the myelin structure in mice a demyelinating inflammatory immune response can be elicited [6], suggesting that altered organization of myelin relates to inflammation causing demyelinating lesions. In MS NAWM, disorganization of the nodes of Ranvier and myelin blistering have been observed [11, 23, 44], and myelin from MS donors obtained from the NAWM is phagocytosed more efficiently compared to myelin obtained from control donors [15]. In the NAWM of MS donors, a disturbance of lipid composition due to a metabolic defect causing an increase in phospholipids and decrease of sphingolipids [43] and deimination of the myelin basic protein (MBP) [28] have been modelled to result in an increased repulsive force between myelin sheaths [28, 43].

Here, we have systematically applied immunohistochemical (IHC) and transmission electron microscopy (TEM) methods on human optic nerve tissue to quantitatively analyze the

characteristics and components of the axon and the myelin in the NAWM in MS at the ultrastructural level. To examine early myelin pathology in MS and the association of immune cell activation, we systematically correlated MS innate and adaptive immune parameters with these NAWM characteristics. We show that in MS optic nerve NAWM, ultrastructural characteristics of the axon-myelin unit are altered. There is a disorganization of the nodes of Ranvier and potassium channels are unmasked, the myelin is less compact, and there are more axonal mitochondria axonal, and this correlates with an increased number of activated and phagocytic microglia and T cells. Together, these sub-clinical alterations may contribute to disease progression in MS.

Methods

Donors and sample collection

Post-mortem optic nerve tissue of n=8 MS donors and n=8 healthy control donors was provided by the Netherlands Brain Bank (NBB, Amsterdam, The Netherlands, www.brainbank.nl). All donors provided informed consent for brain autopsy and for the use of material and clinical data for research purposes in compliance with national ethics guidelines. MS pathology was confirmed by a certified neuropathologist.

At autopsy, if no optic nerve lesions were visible by eye, the optic nerve was dissected at 1-cm distance of the optic chiasm, and each optic nerve sample was cut longitudinally. One half of the tissue was either fixed in formalin and embedded in paraffin (n=8) or fixed for 24 hours in 4% paraformaldehyde and cryo-protected in 30% sucrose prior to freezing (n=8) for high resolution IHC, and the other half of the tissue was fixed in a phosphate buffer with 2.5% glutaraldehyde, 4% paraformaldehyde, and 0.5% NaCl (n=16) for TEM. Axons in the optic nerve are bundled and oriented in the same direction, which allows for the study of axons cut either longitudinally or transverse. All longitudinal and sagittal sections were checked for demyelinated and reactive sites, and donors were excluded when these were present. Thus, optic nerves studied were considered lesion-free (NA)WM.

For MS donors, clinical disability milestones during the disease course were scored following the Kurtze's Expanded Disability Status Scale (EDSS) and the age at onset and the total duration of disease from onset of first symptoms were described. Disease severity score

was calculated as 5 – log (years to EDSS6 + 1). For each MS donor, the lesion load and reactive site load, proportion of active lesions, mixed active/inactive lesions, inactive lesions, and remyelinated lesions, and the microglia macrophage activity score (MMAS) score was calculated as previously described [19, 22].

Sample preparation

For high resolution IHC, 20-µm thick cryo-protected sections were cut longitudinally with a cryostat and stored in phosphate buffered saline (PBS) + 0.1% sodium azide until use. For TEM, samples were treated and contrasted using a modified reduced osmium/tetroxide-thiocarbohydrazide/osmium protocol [42]. Semi-thin (500 nm) and ultra-thin (60 nm) sections were cut transversally with an ultramicrotome. The region of interest was guided by 1:1 methylene blue/Azure II staining of semi-thin sections for 1 minute. Ultra-thin sections were mounted on copper grids.

Immunohistochemistry

For validation of the NAWM of all samples, 8-µm sections of the paraffin-embedded samples were deparaffinized and rehydrated in a xylene and ethanol series and 20-µm cryoprotected sections of the frozen sample were washed in PBS. All primary antibodies and antigen retrieval methods can be found in Table 1.

Sections were incubated with 3% H_2O_2 in PBS + 0.5% TritonX for 10 minutes. Aspecific binding was blocked with blocking buffer (PBS + 10% normal horse serum (NHS) + 1% bovine serum albumin (BSA) + 0.5% TritonX) for 1 hour, and primary antibodies were incubated overnight at 4^{o}C at dilutions indicated in Table 1. Appropriate biotinylated secondary antibodies were incubated for 1 hour 1:400 in blocking buffer and avidin-biotin-complex 1:800 in PBS was incubated for 45 minutes. For HLA, PLP, APP and SMI32, the staining was visualized with DAB, and sections were counterstained with hematoxylin for 30 seconds and dehydrated in ethanol and xylene series. For Kv1.2, biotinylated tyramide was incubated 1:10,000 for 10 minutes, and avidin-biotin-complex 1:800 was incubated for 45 minutes. For all stainings, conjugated fluorophores 1:800 were incubated for 1 hour. Nuclei were stained with Hoechst (1:1.000) for 10 minutes and Sudan Black 0.1% in 70% ethanol was incubated for 10 minutes.

Quantification of immunohistochemistry

For quantification of markers of Wallerian degeneration, scans of the APP and SMI32 staining were made (Axio slide scanner, 20 x magnification) and images were analyzed with Qupath. Donors were marked for presence of APP^+ axonal fragments. For SMI32, the whole tissue section was outlined and a threshold mask was used to quantify the percentage of the tissue positive for dark SMI32 staining. For microglia activity and lymphocyte presence, scans were made of the optic nerve (Axio slide scanner, 20 x magnification). In Qupath, the whole tissue section was outlined, regions with aspecific staining were excluded, and the area of the tissue was measured. For microglia quantification in Qupath, the cell profiler was run on the DAPI signal, cell classifiers were created of the Iba1, CD68, P2RY12, TMEM119, and HLA signal, and composites were created to quantify the number of single or double positives. Distribution of microglia was assessed. For lymphocyte quantification, the number of $CD3^+$ T and $CD19^+$ B cells were counted. All measurements were normalized on the size of the tissue. For $CD3^+$ T cells, percentage of T cells localized in the perivascular space or parenchyma was assessed with laminin.

Quantification of the nodes of Ranvier was performed in ImageJ. The length of 345 control nodes and 257 MS nodes was measured, the length of 974 control paranodes and 692 MS paranodes were measured, and for the juxtaparanodes, the length and percentage of the paranode overlapping the juxtaparanodes were quantified of 82 control juxtaparanodes and 81 MS juxtaparanodes.

Mitochondria and axons were imaged in 3-6 regions of interest per donor at 100 x with the STED microscope (STEDYCON, Abberior Instruments GmbH, Göttingen, Germany). Images were analyzed on Imaris (v. 9.7, Bitplane AG, Zürich, Switzerland). In Imaris, the mitochondria and axons were reconstructed, and a filter removed all mitochondria that did not lie within the axon. The number of axonal mitochondria were measured, and the surface area of the axons and size of axonal mitochondria were measured. The frequency of mitochondria was calculated by calculating the number of mitochondria per μm^2 axon.

Transmission electron microscopy

Images were acquired at 5,000 x and 30,000 x magnification at random regions of interest (ROIs) with a transmission electron microscope (LEO EM912 Omega, Carl Zeiss Microscopy GmbH, Oberkochen, Germany) equipped with a dual speed, wide-angle 2K-CCD camera (TRS,

Moorenweis, Germany) using iTEM (Olympus, Tokyo, Japan) and digitally edited with ImageJ version 2.1.0 [34].

Per donor, 119-268 myelinated axons were analyzed at 5,000 x magnification using a grid for unbiased quantification to characterize the g-ratio, myelin density, axon caliber, and inner tongue area. The diameter of the axon, the inner tongue, and the myelin sheath were calculated based on the area. The g-ratio was calculated by dividing the diameter of the axon with the diameter of the myelin sheath corrected for the inner tongue [26]. The myelin density was calculated with a positive pixel classifier in QuPath [5]. Per donor, in six randomly selected images at 5,000 x magnification, the number of myelinated axons were counted and the number of myelinoid bodies, outfoldings, and mitochondria per axon was calculated. Additionally, of axons with visible mitochondria the percentage of the axon covered by the area of the mitochondria was calculated. Of 16-30 axons per donor, the peri-axonal space was measured at 30,000 x magnification. For the MS donors, the ultrastructural characteristics were correlated with the clinical and pathological MS characteristics.

Statistical analysis

Considering the small group size, correlations between continuous averages per donor were tested with Spearman correlation coefficient. Differences in donor demographics and averages of ultrastructural characteristics were tested between groups with a two-sided Student's T-test. If multiple measurements were made per donor for IHC or TEM characteristics, these were tested with a linear mixed-effect model correcting for within-donor measurements. All statistics were performed in RStudio Desktop (version 1.2.5033, Rstudio, Inc., Boston, MA, USA), using key packages ggplot2, lme4, car, plyr, ggpubr, Hmisc, and corrplot. P-values <0.05 were considered significant.

Results

Donor demographics

Donors with demyelination of the optic nerve, as assessed with PLP and Luxol Fast Blue (LFB), or with reactive sites, as seen with KiM1P staining, were excluded from the study, resulting in a cohort of n=8 control donors and n=8 MS donors. Microglia nodules were seen in both

groups (Fig. 1A-C) and were avoided for quantification of ultrastructural characteristics. 6 control donors and 3 MS donors had cataract or macular degeneration and one MS donor had a prior history of optic neuritis in the contralateral optic nerve. As assessed with APP and SMI32, there was a comparable prevalence of Wallerian degeneration in controls compared to MS (Fig. 1D-H). Demographics and characteristics for disease severity and pathology of the MS donors are summarized in Table 2. In the IHC dataset, the groups were matched for age, post-mortem delay (PMD) and pH of the CSF, however there were significantly more control females than females with MS (CON: 100%, MS: 25%, p=0.03). In the TEM dataset, the groups were matched for PMD and pH of the CSF, however the MS donors were significantly younger than the control donors (CON: 85.88 ± 6.38 years, MS: 70.13 ± 7.22 years, p=4.1e-4) and there were significantly less females with MS than control females (CON: 100% female, MS: 50% female, p=0.02). The cause of death of control donors was cancer (n=3), old age (n=1), infection (n=1), heart failure (n=1), palliative sedation (n=1) or euthanasia (n=1). The cause of death of MS donors was infection (n=3), euthanasia (n=3), palliative sedation (n=1) or respiratory insufficiency (n=1).

More active microglia and lymphocytes in MS NAWM

To determine activity of microglia of the NAWM of MS and control donors, the optic nerve was quantified for microglia activity as assessed with P2RY12/HLA and iba1/CD68. Lymphocyte presence was quantified with CD3, CD19, and CD138 staining. In MS compared to controls, there were similar numbers of microglia ($Iba1^+CD68$) and there were more activated, phagocytic microglia ($Iba1^+CD68^+$, CON: 234.55 ± 22.91 cells/mm^2, MS: 340.06 ± 45.65 cells/mm^2, p=0.01). Furthermore, there was a comparable number of homeostatic microglia ($P2RY12^+HLA^-$) and partially activated microglia ($P2RY12^+HLA^+$). Interestingly, there were more activated microglia ($P2RY12^-HLA^+$, CON: 257.06 ± 35.32 cells/mm^2, MS: 486.61 ± 133.11 cells/mm^2, p=0.04), despite the higher age of control patients. The microglia activity was homogeneously distributed throughout the optic nerve tissue. In MS compared to controls, there were more $CD3^+$ T cells (CON: 14.45 ± 2.23 cells/mm^2, MS: 29.70 ± 8.76 cells/mm^2, p=0.04). No cuffing, defined as more than one ring of perivascular CD3+ T cells [31], was observed in the tissue. As assessed with laminin, an equal percentage of the $CD3^+$ T cells were localized in the parenchyma in MS compared to controls (CON: 7.82%, MS: 11.57%) (Fig. 1I-S). Only 1 MS donor showed the presence of $CD19^+$ B cells (data not shown). Thus,

consistent with previous findings [10, 14, 46], the NAWM in MS is characterized by substantial activated immune cell infiltration and activated resident immune cells.

Elongation and unmasking of ion channels at nodes of Ranvier in MS NAWM

With high resolution IHC, the organization of the nodes (75 per donor), paranodes (208 per donor), and juxtaparanodes (20 per donor) was quantified (illustration at Fig. 2A). Representative images of nodes and paranodes are visualized in Fig. 2B. In MS compared to controls, the length of the nodes was not different however the length of CASPR1 was longer (CON: 3.36 ± 0.52 µm, MS: 4.51 ± 0.94 µm, p=0.03, Fig. 2C-D). A representative image of a non-overlapping paranode and juxtaparanode is shown in Fig. 2E with the corresponding intensity graph in Fig. 2F, and a largely overlapping paranode and juxtaparanode is visualized in Fig. 2G with the corresponding intensity graph in Fig. 2H. In MS compared to controls, the Kv1.2 ion channel-positive area was significantly longer (CON: 4.74 ± 0.52 µm, MS: 6.12 ± 1.11 µm, p=0.01), and the percentage of CASPR1-positive area overlapping with Kv1.2 staining is larger (CON: 34.50% ± 2.23%, MS: 49.30% ± 6.29%, p=7.12e-5, Fig. 2I-J). Thus, similar to others [11, 44], here we showed that the nodes of Ranvier are disorganized as there is elongation of the paranodes and juxtaparanodes and increased overlap between the paranodal and juxtaparanodal regions.

Correlation between ultrastructural characteristics in MS NAWM

In Fig. 3A-C, representative TEM images are shown. All Spearman correlations between ultrastructural characteristics and age, post-mortem delay (PMD), and pH are visualized in Fig. 3D, with significant p-values indicated in text and correlation coefficients indicated in a color scale. The g-ratio, axon caliber, inner tongue area, axonal density, number of outfoldings, number of myelinoid bodies, coverage of the axon by mitochondria, mitochondria frequency, and peri-axonal space were not correlated to age, PMD, and pH of the CSF, and there were no sex differences. The axon caliber was positively correlated to the g-ratio (Fig. 3E, p=0.01, r=0.63), the inner tongue area (p=0.02, r=0.57), and the number of outfoldings (p=2.5e-3, r=0.70). The axon caliber was negatively correlated to the axonal density (Fig. 3F, p=6.9e-5, r=-0.83) and the coverage of the axon by mitochondria (p=0.02, r=-0.56). The axonal density was negatively correlated with the number of outfoldings (p=0.01, r=-0.65) and positively correlated with the coverage of the axon by mitochondria (p=0.01, r=0.63).

Ultrastructural alterations of the myelin in MS NAWM

The ultrastructural characteristics based on 119-268 myelinated axons per donor, or 16-30 myelinated axons per donor for the peri-axonal space, were quantified with TEM and compared between MS and controls. The axon caliber was not different in MS NAWM compared to control WM (Fig. 4A). In MS NAWM, there was a significantly lower g-ratio compared to controls (CON: 0.53 ± 0.03, MS: 0.50 ± 0.04, p=0.03) and a lower myelin density (CON: 95.43% ± 1.47%, MS: 92.43% ± 3.01%, p=0.01) (Fig. 4B-C). The inner tongue area and peri-axonal space were not different in MS NAWM compared to control WM (Fig. 4D-E). The number of myelinoid bodies, axonal density, and the number of outfoldings were not different between MS and controls (Fig. 4F-H). Therefore, there are ultrastructural myelin alterations in MS as the myelin is less compact in MS NAWM compared to control WM.

Increase of axonal mitochondria in MS NAWM

To fully appreciate the 3-dimentional (3D) shape of mitochondria, their frequency and size were studied with both TEM and high resolution IHC. As assessed with EM, in MS a higher percentage of axons containing mitochondria was visible (CON: 18.41% ± 5.68%, MS: 23.68% ± 3.72%, p<0.05), however in axons containing mitochondria the percentage mitochondrial coverage of the axons was not different between MS and controls (Fig. 5A-C). High resolution immunohistochemical stainings of axonal mitochondria were reconstructed in Imaris as visualized in Fig. 5D. Compared to healthy control WM, in MS axons in the NAWM contained more mitochondria (CON: 0.05 ± 0.01, MS: 0.09 ± 0.01, p=1.5e-4), however the surface area of the mitochondria was not different (Fig. 5E-F). This implies a higher axonal energy demand or a stagnated mitochondrial transport in MS NAWM compared to control WM.

Ultrastructural abnormalities correlate with microglia activity markers and T cell number

Ultrastructural characteristics as measured with TEM and IHC that were significantly different in MS compared to controls were tested for correlation with microglia activity and lymphocyte presence as visualized in Fig. 6. The g-ratio was near-significantly negatively correlated to the number of $P2RY12^{-}HLA^{+}$ activated microglia and the number of $CD3^{+}$ T cells (p=0.071, r=-0.67; p=0.071, r=-0.67) and was not correlated to the number of $Iba1^{+}CD68^{+}$ phagocytic microglia (p=0.120, r=-0.56, data not shown). The myelin density was negatively correlated to the

number of P2RY12^{-}HLA^{+} activated microglia (p=0.001, r=-0.93), the number of Iba1^{+}CD68^{+} phagocytic microglia (p=0.007, r=-0.86) and the number of CD3^{+} T cells (p=0.047, r=-0.74) (Fig. 6A-C). The axonal mitochondria frequency was positively correlated to the number of P2RY12^{-}HLA^{+} activated microglia (p=0.015, r=0.81) and the number of Iba1^{+}CD68^{+} phagocytic microglia (p=0.047, r=0.71) (Fig. 6D-E), and was not correlated to the number of CD3^{+} T cells. The paranode length was not correlated to the number of P2RY12^{-}HLA^{+} activated microglia or the number of Iba1^{+}CD68^{+} phagocytic microglia and was positively correlated to the number of CD3^{+} T cells (p=0.015, r=0.81 (Fig. 6F). The juxtaparanode length was positively correlated to the number of P2RY12^{-}HLA^{+} activated microglia (p=0.021, r=0.79) (Fig. 6G), was approaching a positive correlation to the number of Iba1^{+}CD68^{+} phagocytic microglia (data not shown, p=0.058, r=0.69), and was positively correlated to the number of CD3^{+} T cells (p=0.015, r=0.81) (Fig. 6H). The percentage overlap between the paranodes and juxtaparanodes was positively correlated to the number of P2RY12^{-}HLA^{+} activated microglia (p=0.021, r=0.79), the number of Iba1^{+}CD68^{+} phagocytic microglia (p=0.015, r=0.81) and the number of CD3^{+} T cells (p=0.015, r=0.81) (Fig. 6I-K).

The g-ratio, myelin density, axonal mitochondria frequency, length of CASPR1, length of Kv1.2, and percentage overlap of CASPR1 with Kv1.2 were not correlated to the lesion load, MMAS score, severity score nor the percentage of SMI32^{+} axons (data not shown).

Discussion

Here, we present the first systematic quantification of ultrastructural characteristics of the NAWM of control and MS donors using TEM and high-resolution IHC. In the NAWM of the optic nerve in MS compared to controls, we found an elongation of the paranodes and juxtaparanodes and an increased overlap of paranodes and juxtaparanodes, causing unmasking of the potassium channels, similar to previous findings in subcortical NAWM [11, 44]. We further observed that the g-ratio is lower and that myelin is less compact, and that there is a higher frequency of mitochondria. The characteristics that are altered in MS are furthermore correlated positively with the number of active (P2RY12^{-}HLA^{+}) and phagocytic (Iba1^{+}CD68^{+}) microglia and the number of CD3^{+} T cells present in the tissue. The loss of microglia homeostasis and presence of lymphocytes may be causal to alterations in the axon-myelin unit that could lead to more axonal mitochondria and possibly subsequently more free

radicals that can oxidize the lipids, making the myelin more prone to phagocytosis and therefore predisposing the tissue for lesion formation.

Ultrastructural and immunohistochemical characteristics of the NAWM were not confounded by donor demographics nor were they correlated with MS pathology throughout the CNS. Though the MS and control group differed in age and sex, no correlation between age and the data was found nor were there any sex-related differences in the data. In MS and control donors there was a similar prevalence of Wallerian degeneration and the percentage of $SMI32^{+}$ axons was not correlated to the data. Therefore, the data were not affected by Wallerian degeneration. Sampling bias was minimized by random selection of ROIs and using a grid for TEM axon analysis. Due to methodological challenges of performing TEM on human tissue, not much yet is known about the ultrastructural characteristics of human WM. Here, potentially due to the short post-mortem delay and direct fixation at autopsy, tissue was well preserved enabling systematical quantification of ultrastructural characteristics. For ultrastructural characteristics quantified with IHC, all stainings were tripled with microglia staining to ensure exclusion of regions with small clusters of microglia as local pro-inflammatory sites may skew the data. Donors with macroscopically visible lesions in the optic nerve during autopsy and donors with focal lesion pathology in the sampled area of the optic nerve, as assessed with Kim1P, PLP, Bielschowsky, and Luxol Fast Blue staining, were excluded. Of the included donors, one MS donor had a history of optic neuritis in the opposing optic nerve, some control and some MS donors had cataract or macular degeneration, and no other donors had mentioning of optic neuritis in their clinical files.

In line with previous studies on subcortical WM on the nodes of Ranvier, in MS the length of the node was similar between MS and controls and in MS the paranode as well as the juxtaparanode were longer compared to controls, with a larger overlap of the paranode and the juxtaparanode [8, 11, 16, 32, 44]. We and others show that the extent of abnormalities at the nodes of Ranvier in the NAWM is correlated to the degree of microglial activation [16], and previously, it was shown that these alterations can be provoked *in vitro* by pro-inflammatory cytokines [11]. The unmasking of potassium channels may contribute to altered electrical properties of the axons [41] and altered potassium release can modulate microglia-node interactions [32].

In line with previous electron microscopy studies on non-human tissue [26, 38, 39], the axon caliber was positively correlated with the g-ratio, indicating that the myelin diameter

corrected for the inner tongue is relative to the axonal diameter. Surprisingly, in MS, we found a smaller g-ratio compared to controls. As we found no difference in axon caliber, inner tongue area, or peri-axonal space between MS and controls, the altered g-ratio in MS can most likely be attributed to changes in the myelin itself. As the myelin density of MS donors is lower compared to control donors, it is likely that the smaller g-ratio in MS is due to less compact wrapping of the myelin. Previously, larger g-ratios were found in the normal-appearing grey matter of MS donors compared to controls, which was attributed to extensive remyelination [1]. Indeed, we did not observe remyelination in the NAWM of the optic nerves and the NAWM in MS seems to be affected pathologically different compared to the normal appearing grey matter. Moreover, an abnormal sphingolipid metabolism was found in MS NAWM [17, 25, 27], perhaps mediated by pro-inflammatory cytokines [35], and the increased lipid peroxidation products 4-HNE modified lysine and histidine as well as deimination of myelin basic protein were modeled to result in an increase in the repulsive force between myelin layers, leading to decompaction of the myelin structure [28, 43]. This altered sphingolipid metabolism may be the mechanism underlying the lower g-ratio and lower myelin compactness in MS that we have shown here. Myelin isolated from the NAWM was previously shown to be more efficiently phagocytosed by primary human microglia than control myelin [15], indicating that alterations in the myelin may predispose MS myelin for phagocytosis. We speculate that the less compact wrapping of the myelin, the detachment of the myelin at the paranode, and the unmasking of the potassium channels may underly a higher axonal energy demand.

Interestingly, in MS compared to controls, the axons contained a higher number of mitochondria with comparable surface area, which was shown with TEM and as well as with 3D IHC to fully appreciate the highly dynamic structure of mitochondria. This implies that there is a higher energy demand of the axon in MS than controls or that the transport of mitochondria along the axon has stagnated, perhaps due to nodal pathology [11, 16]. Although most mitochondria in axons are stationary, they will rapidly redistribute to sites of pathological stress [40]. During metabolic or environmental stress of a cell, mitochondrial fusion and fission help mitigate stress, create new mitochondria, and enable removal of damaged mitochondria [45]. If mitochondrial fragmentation occurs while surface area remains constant, this can result in a higher concentration of calcium, resulting in higher mitochondrial activity and more ATP production [12]. This improved calcium buffering

capacity may provide a neuroprotective opportunity [21, 33], however this could additionally lead to an increase of free radicals which, when in pathological amounts, can cause damage to the mitochondria itself and to the tissue surrounding it [18]. These radicals are additionally produced in large amounts by activated microglia, and mitochondrial injury is considered a key element of neurodegeneration in MS [20].

In line with previous studies in the NAWM of MS, there was a higher number of activated microglia ($P2RY12^{-}HLA^{+}$), phagocytic microglia ($Iba1^{+}CD68^{+}$) and $CD3^{+}$ T cells per square millimeter tissue compared to controls [14, 36, 46]. The percentage of parenchymal $CD3^{+}$ T cells was similar in controls and MS, which is in line with the localization of subcortical (NA)WM T cells [10]. The number of active and phagocytic microglia and $CD3^{+}$ T cells were accordingly correlated to ultrastructural characteristics of the NAWM in the same direction as these characteristics were affected in MS compared to controls. Previous studies have shown that pro-inflammatory cytokines that can be produced by these immune cells *in vitro* lead to elongation and disorganization of the nodes of Ranvier, and the extent of *ex vivo* lipid metabolism defect in MS is related to evidence of monocyte infiltrates [11, 43]. As ultrastructural characteristics were not correlated to characteristics of MS pathology in the CNS of the donors, it is likely that the abnormalities seen here in the NAWM of the optic nerve in MS are driven by pro-inflammatory cytokines produced by lymphocytes and active and phagocytic microglia rather than by Wallerian degeneration. However, it is also possible that ultrastructural abnormalities could lead to increased immune activity, therefore future research is necessary to elucidate any causalities. It should be noted that we cannot exclude the presence of lesions in tissue distally in the optic nerve, nor can we exclude the possibility that the smaller group size reduced the power thus far that no correlations could be found between ultrastructural characteristics and MS pathology or the severity score. It is likely that in MS at local inflammatory sites in the NAWM, such as microglia nodules or inflamed vessels, more ultrastructural axonal characteristics will be altered, and the interaction of immune cells and the axon-myelin unit may also be of importance. Future research should shed light on this.

Taken together, our data show ultrastructural changes in the NAWM of MS at the levels of the myelin and axon including a less compact myelin composition, disorganization of the nodes of Ranvier and increased axonal mitochondria frequency in progressive MS. Moreover,

the changes correlated with chronic inflammation throughout the CNS. These changes may contribute to further MS progression.

Acknowledgements

We are grateful to the brain donors and their families for their commitment to the Netherlands Brain Bank donor program. We thank Houson Li (University of Göttingen), Jeen Engelenburg, Marlijn van der Poel, and Manon Vincenten (Netherlands institute for Neuroscience) for their intellectual input and technical help. Funding for this research was obtained from MS Research grants 17-975 and 19-1079 (MoveS), Vici grant 865.17.003 from the Netherlands Research Council (NWO), the ERC (MyeliNANO), and the Adelson Medical Research Foundation (AMRF).

Author contributions

AB, SH, AS, CS, KN, MK, WM and IH contributed to conception and design of the study; AB, SH and TR contributed to acquisition and analysis of data; AB, SH, AS, TR, JH, JS, KN, CS, MK, WM and IH contributed to drafting and editing the text and figures.

Potential conflicts of interest

The authors have no conflicts of interest to declare

Data availability

All images will be stored at Groningen database (Nanotamy).

References

1. Albert M, Antel J, Brück W, Stadelmann C (2007) Extensive cortical remyelination in patients with chronic multiple sclerosis. Brain Pathol 17:129–138. doi: 10.1111/j.1750-3639.2006.00043.x
2. Allen I V., McKeown SR (1979) A histological, histochemical and biochemical study of the macroscopically normal white matter in multiple sclerosis. J Neurol Sci 41:81–91. doi: 10.1016/0022-510X(79)90142-4
3. Allen I V., McQuaid S, Mirakhur M, Nevin G (2001) Pathological abnormalities in the normal-appearing white matter in multiple sclerosis. Neurol Sci 22:141–144. doi: 10.1007/s100720170012
4. Bando Y, Nomura T, Bochimoto H, Murakami K, Tanaka T, Watanabe T, Yoshida S (2015) Abnormal morphology of myelin and axon pathology in murine models of multiple sclerosis. Neurochem Int 81:16–27. doi: 10.1016/j.neuint.2015.01.002
5. Bankhead P, Loughrey MB, Fernández JA, Dombrowski Y, McArt DG, Dunne PD, McQuaid S, Gray RT, Murray LJ, Coleman HG, James JA, Salto-Tellez M, Hamilton PW (2017) QuPath: Open source software for digital pathology image analysis. Sci Rep 7:1–7. doi: 10.1038/s41598-017-17204-5
6. Caprariello A V., Rogers JA, Morgan ML, Hoghooghi V, Plemel JR, Koebel A, Tsutsui S, Dunn JF, Kotra LP, Ousman SS, Wee Yong V, Stys PK (2018) Biochemically altered myelin triggers autoimmune demyelination. Proc Natl Acad Sci U S A 115:5528–5533. doi: 10.1073/pnas.1721115115
7. Cohen CCH, Popovic MA, Klooster J, Weil MT, Möbius W, Nave KA, Kole MHP (2020) Saltatory Conduction along Myelinated Axons Involves a Periaxonal Nanocircuit. Cell 180:311-322.e15. doi: 10.1016/j.cell.2019.11.039
8. Coman I, Aigrot MS, Seilhean D, Reynolds R, Girault JA, Zalc B, Lubetzki C (2006) Nodal, paranodal and juxtaparanodal axonal proteins during demyelination and remyelination in multiple sclerosis. Brain 129:3186–3195. doi: 10.1093/brain/awl144
9. Fraher J, Dockery P (1998) A strong myelin thickness-axon size correlation emerges in developing nerves despite independent growth of both parameters. J Anat 193:195–201. doi: 10.1046/j.1469-7580.1998.19320195.x
10. Fransen NL, Hsiao C-C, van der Poel M, Remmerswaal EBM, Kuhlmann T, Mason MRJ, Hamann J, Smolders J, Huitinga I (2020) Tissue-resident memory T cells invade the brain parenchyma in multiple sclerosis white matter lesions. Brain in press
11. Gallego-Delgado P, James R, Browne E, Meng J, Umashankar S, Tan L, Picon C, Mazarakis ND, Faisal AA, Howell OW, Reynolds R (2020) Neuroinflammation in the normal-appearing white matter (NAWM) of the multiple sclerosis brain causes abnormalities at the nodes of Ranvier
12. Gottlieb RA, Piplani H, Sin J, Sawaged S, Hamid SM, Taylor DJ, de Freitas Germano J (2021) At the heart of mitochondrial quality control: many roads to the top. Cell Mol Life Sci 78:3791–3801. doi: 10.1007/s00018-021-03772-3
13. Haider L, Fischer MT, Frischer JM, Bauer J, Höftberger R, Botond G, Esterbauer H, Binder CJ, Witztum JL, Lassmann H (2011) Oxidative damage in multiple sclerosis lesions. Brain 134:1914–1924. doi: 10.1093/brain/awr128
14. Hendrickx DAE, van Eden CG, Schuurman KG, Hamann J, Huitinga I (2017) Staining of HLA-DR, Iba1 and CD68 in human microglia reveals partially overlapping expression

depending on cellular morphology and pathology. J Neuroimmunol 309:12–22. doi: 10.1016/j.jneuroim.2017.04.007

15. Hendrickx DAE, Schuurman KG, van Draanen M, Hamann J, Huitinga I (2014) Enhanced uptake of multiple sclerosis-derived myelin by THP-1 macrophages and primary human microglia. J Neuroinflammation 11:1–11. doi: 10.1186/1742-2094-11-64
16. Howell OW, Rundle JL, Garg A, Komada M (2015) Activated microglia mediate axo-glial disruption that contributes to axonal injury in multiple sclerosis. J Neuropathol Exp Neurol 69:1017–1033. doi: 10.1097/NEN.0b013e3181f3a5b1.Activated
17. Jana A, Pahan K (2010) Sphingolipids in multiple sclerosis. NeuroMolecular Med 12:351–361. doi: 10.1007/s12017-010-8128-4
18. Kozin MS, Kulakova OG, Favorova OO (2018) Involvement of Mitochondria in Neurodegeneration. Biochemistry 83:1002-1021.
19. Kuhlmann T, Ludwin S, Prat A, Antel J, Brück W, Lassmann H (2017) An updated histological classification system for multiple sclerosis lesions. Acta Neuropathol 133:13–24. doi: 10.1007/s00401-016-1653-y
20. Lassmann H, Van Horssen J (2011) The molecular basis of neurodegeneration in multiple sclerosis. FEBS Lett 585:3715–3723. doi: 10.1016/j.febslet.2011.08.004
21. Licht-Mayer S, Campbell GR, Canizares M, Mehta AR, Gane AB, McGill K, Ghosh A, Fullerton A, Menezes N, Dean J, Dunham J, Al-Azki S, Pryce G, Zandee S, Zhao C, Kipp M, Smith KJ, Baker D, Altmann D, Anderton SM, Kap YS, Laman JD, Hart BA'., Rodriguez M, Watzlawick R, Schwab JM, Carter R, Morton N, Zagnoni M, Franklin RJM, Mitchell R, Fleetwood-Walker S, Lyons DA, Chandran S, Lassmann H, Trapp BD, Mahad DJ (2020) Enhanced axonal response of mitochondria to demyelination offers neuroprotection: implications for multiple sclerosis. Acta Neuropathol 140:143–167. doi: 10.1007/s00401-020-02179-x
22. Luchetti S, Fransen NL, van Eden CG, Ramaglia V, Mason M, Huitinga I (2018) Progressive multiple sclerosis patients show substantial lesion activity that correlates with clinical disease severity and sex: a retrospective autopsy cohort analysis. Acta Neuropathol 135:511–528. doi: 10.1007/s00401-018-1818-y
23. Luchicchi A, Hart B, Frigerio I, van Dam AM, Perna L, Offerhaus HL, Stys PK, Schenk GJ, Geurts JJG (2021) Axon-Myelin Unit Blistering as Early Event in MS Normal Appearing White Matter. Ann Neurol 89:711–725. doi: 10.1002/ana.26014
24. Ludwin SK (2006) The pathogenesis of multiple sclerosis: Relating human pathology to experimental studies. J Neuropathol Exp Neurol 65:305–318. doi: 10.1097/01.jnen.0000225024.12074.80
25. Marbois BN, Faull KF, Fluharty AL, Raval-Fernandes S, Rome LH (2000) Analysis of sulfatide from rat cerebellum and multiple sclerosis white matter by negative ion electrospray mass spectrometry. Biochim Biophys Acta - Mol Cell Biol Lipids 1484:59–70. doi: 10.1016/S1388-1981(99)00201-2
26. Meschkat M, Steyer AM, Weil M-T, Kusch K, Jahn O, Piepkorn L, Agüi-Gonzalez P, Phan NTN, Ruhwedel T, Sadowski B, Rizzoli SO, Werner HB, Ehrenreich H, Nave K-A, Möbius W (2022) White matter integrity in mice requires continuous myelin synthesis at the inner tongue. Nat Commun 13. doi: 10.1038/s41467-022-28720-y
27. Moscatelli EA, Isaacson E (1969) Gas liquid chromatographic analysis of sphingosine bases in sphingolipids of human normal and multiple sclerosis cerebral white matter. Lipids 4:550–555. doi: 10.1007/BF02531040
28. Musse AA, Boggs JM, Harauz G (2006) Deimination of membrane-bound myelin basic

protein in multiple sclerosis exposes an immunodominant epitope. Proc Natl Acad Sci U S A 103:4422–4427. doi: 10.1073/pnas.0509158103
29. Nave KA, Werner HB (2014) Myelination of the nervous system: Mechanisms and functions. Annu Rev Cell Dev Biol 30:503–533. doi: 10.1146/annurev-cellbio-100913-013101
30. van der Poel M, Ulas T, Mizee MR, Hsiao CC, Miedema SSM, Adelia, Schuurman KG, Helder B, Tas SW, Schultze JL, Hamann J, Huitinga I (2019) Transcriptional profiling of human microglia reveals grey–white matter heterogeneity and multiple sclerosis-associated changes. Nat Commun 10:1–13. doi: 10.1038/s41467-019-08976-7
31. Revesz T, Kidd D, Thompson AJ, Barnard RO, Mcdonald WI (1994) A comparison of the pathology of primary and secondary progressive multiple sclerosis. Brain 117:759–765. doi: 10.1093/brain/117.4.759
32. Ronzano R, Roux T, Thetiot M, Aigrot MS, Richard L, Lejeune FX, Mazuir E, Vallat JM, Lubetzki C, Desmazières A (2021) Microglia-neuron interaction at nodes of Ranvier depends on neuronal activity through potassium release and contributes to remyelination. Nat Commun 12. doi: 10.1038/s41467-021-25486-7
33. Rosenkranz SC, Shaposhnykov AA, Träger S, Engler JB, Witte ME, Roth V, Vieira V, Paauw N, Bauer S, Schwencke-Westphal C, Schubert C, Bal LC, Schattling B, Pless O, van Horssen J, Freichel M, Friese MA (2021) Enhancing mitochondrial activity in neurons protects against neurodegeneration in a mouse model of multiple sclerosis. Elife 10:1–60. doi: 10.7554/eLife.61798
34. Schindelin J, Arganda-Carreras I, Frise E, Kaynig V, Longair M, Pietzsch T, Preibisch S, Rueden C, Saalfeld S, Schmid B, Tinevez JY, White DJ, Hartenstein V, Eliceiri K, Tomancak P, Cardona A (2012) Fiji: An open-source platform for biological-image analysis. Nat Methods 9:676–682. doi: 10.1038/nmeth.2019
35. Singh I, Pahan K, Khan M, Singh AK (1998) Cytokine-mediated induction of ceramide production is redox-sensitive: Implications to proinflammatory cytokine-mediated apoptosis in demyelinating diseases. J Biol Chem 273:20354–20362. doi: 10.1074/jbc.273.32.20354
36. Smolders J, Heutinck KM, Fransen NL, Remmerswaal EBM, Hombrink P, ten Berge IJM, van Lier RAW, Huitinga I, Hamann J (2018) Tissue-resident memory T cells populate the human brain. Nat Commun 9:4593. doi: 10.1038/s41467-018-07053-9
37. Snaidero N, Simons M (2014) Myelination at a glance. J Cell Sci 127:2999–3004. doi: 10.1242/jcs.151043
38. Stassart RM, Möbius W, Nave KA, Edgar JM (2018) The Axon-Myelin unit in development and degenerative disease. Front Neurosci 12. doi: 10.3389/fnins.2018.00467
39. Stikov N, Campbell JSW, Stroh T, Lavelée M, Frey S, Novek J, Nuara S, Ho MK, Bedell BJ, Dougherty RF, Leppert IR, Boudreau M, Narayanan S, Duval T, Cohen-Adad J, Picard PA, Gasecka A, CÔté D, Pike GB (2015) Quantitative analysis of the myelin g-ratio from electron microscopy images of the macaque corpus callosum. Data Br 4:368–373. doi: 10.1016/j.dib.2015.05.019
40. Wang B, Huang M, Shang D, Yan X, Zhao B, Zhang X (2021) Mitochondrial Behavior in Axon Degeneration and Regeneration. Front Aging Neurosci 13:1–17. doi: 10.3389/fnagi.2021.650038
41. Waxman S (2005) Multiple Sclerosis as A Neuronal Disease. Elsevier Inc.
42. Webb RI, Schieber NL (2018) Volume Scanning Electron Microscopy: Serial Block-Face

Scanning Electron Microscopy Focussed Ion Beam Scanning Electron Microscopy. In: E. Hanssen (Ed.), Cellular imaging, Biological and medical physics, biomedical engineering. Springer, pp 117–148

43. Wheeler D, Bandaru VVR, Calabresi PA, Nath A, Haughey NJ (2008) A defect of sphingolipid metabolism modifies the properties of normal appearing white matter in multiple sclerosis. Brain 131:3092–3102. doi: 10.1093/brain/awn190
44. Wolswijk G, Balesar R (2003) Changes in the 'expression and localization of the paranodal protein Caspr on axons in chronic multiple sclerosis. Brain 126:1638–1649. doi: 10.1093/brain/awg151
45. Youle RJ, Van Der Bliek AM (2012) Mitochondrial Fission, Fusion, and Stress. Science (80-) 337:1062–1065. doi: 10.1126/science.1219855.Mitochondrial
46. Zrzavy T, Hametner S, Wimmer I, Butovsky O, Weiner, Howard L, Lassmann H, Weiner HL, Lassmann H (2017) Loss of "homeostatic" microglia and patterns of their activation in multiple sclerosis. Brain 140:1900–1913. doi: 10.1093/brain/awx113

Figure legends

Figure 1: Inflammation occurring in the NAWM. (A) Luxol Fast Blue, **(B)** PLP, and **(C)** Kim1p stainings of the optic nerve shows no demyelination or reactive sites, besides from some nodules, with a scale bar of 400 nm. **(D)** APP^+ axonal fragments **(E)** were found in both control and MS tissue. **(F)** $SMI32^+$ axons were observed in both control as **(G)** MS tissue, and **(H)** the percentage of tissue that was $SMI32^+$ was comparable in control and MS tissue. **(I)** Iba1 (in green) and CD68 (in yellow) staining of a control optic nerve with an enlarged panel with an arrow pointing to an $Iba1^+CD68^-$ cell. **(J)** Iba1 (in green) and CD68 (in yellow) staining of an MS optic nerve with an enlarged panel with an arrow pointing to an $Iba1^+CD68^+$ cell. **(K)** In MS compared to controls, there are an equal amount of $Iba1^+$ microglia/mm^2 and more $Iba1^+CD68^+$ microglia/mm^2 ($p=0.01$). (**L**) HLA (in green) and P2RY12 (in yellow) staining of control optic nerve with two enlarged panels, with in the first panel an arrow pointing to a $P2RY12^+HLA^-$ cell and in the second panel an arrow pointing to a $P2RY12^+HLA^+$ cell. **(M)** HLA (in green) and P2RY12 (in yellow) staining of MS optic nerve with two enlarged panels, in the first panel an arrow pointing to a $P2RY12^+HLA^+$ cell and in the second panel an arrow pointing to a $P2RY12^-HLA^+$. **(N)** In MS compared to controls, there are equal numbers of $P2RY12^+HLA^-$ and $P2RY12^+HLA^+$ microglia/mm^2 and more $P2RY12^-HLA^+$ microglia/mm^2 ($p=0.04$). **(O)** CD3 (in yellow) staining of control optic nerve and **(P)** CD3 (in yellow) staining of MS optic nerve with arrows pointing to $CD3^+$ T cells. **(Q)** In MS compared to controls, there are more $CD3^+$ T cells/mm^2 ($p=0.04$). **(R)** As assessed with laminin (in green), $CD3^+$ T cells (in yellow) were found both in the perivascular space as well as in the parenchyma, and **(S)** the percentage of $CD3^+$ T cells in the parenchyma was similar in MS compared to controls.

Figure 2: Altered length and distribution of ion channels at the nodes of Ranvier. (A) Illustrative image showing nodal, paranodal, and juxtaparanodal area. (**B**) Representative images of a control paranode (CASPR1) in the top panel and an MS paranode in the bottom panel. **(C)** In MS, the length of the nodes is comparable to controls, and **(D)** the paranodes (CASPR1) are longer ($p=0.03$). Representative image of (**E**) a control juxtaparanode (Kv1.2, yellow) and paranode (CASPR1, red) not overlapping with (**F**) corresponding intensity plot and of (**G**) an MS juxtaparanode (Kv1.2, yellow) and paranode (CASPR1, red) with high overlap with

(**H**) corresponding intensity plot. In MS compared to controls, (**I**) the juxtaparanodes (Kv1.2) are longer (p=0.01) and (**J**) there is a higher percentage of paranodes (CASPR1) overlapping with juxtaparanodes (Kv1.2) (p=7.12e-5).

Figure 3: Quantification of ultrastructural characterization of the NAWM in the optic nerve. (**A**) TEM image of an MS optic nerve at 5,000 x with indicated a myelin outfolding indicated with a white arrow, axons in blue, inner tongues in yellow, myelin in purple, a myelinoid body with an asterisk, and a mitochondria indicated with an arrowhead. (**B**) Representative image of 5,000 x TEM image showing quantification of myelin density with the top panel showing a control myelin ring with high density and the lower panel showing MS myelin with low density. **(C)** Transmission electron microscope image at 30,000 x with the peri-axonal space in orange. (**D**) Correlation matrix of Spearman's correlations of ultrastructural characteristics measured with the TEM and donor demographics, showing that the axon calibre correlates positively to the g-ratio, the inner tongue area, and the number of outfoldings and negatively to the axon density. The axon density correlates negatively to the inner tongue area and the number of outfoldings and positively to the mitochondrial coverage of the axon. The number of outfoldings correlates negatively to the mitochondrial coverage of the axon. (**D**) The axon calibre correlates positively to the g-ratio (p=0.009, r=0.63) and (**E**) negatively to the axonal density (p=6.9e-5, r=-0.83).

Figure 4: Less compact myelin wrapping in MS NAWM. In MS compared to controls, (**A**) the axon calibre was similar, (**B**) the g-ratio was smaller (p=0.02), (**C**) the myelin density was smaller (p=0.01), (**D**) the inner tongue area was similar, and (**E**) the peri-axonal space was similar. There were no differences between MS and controls in (**F**) amount of myelinoid bodies, (**G**) the axonal density, or (**H**) the amount of outfoldings.

Figure 5: Increased number of axonal mitochondria in MS NAWM. (**A**) TEM image taken at 5,000 x with two enlarged panels, the top showing an axon with no mitochondria visible, the bottom showing an axon with mitochondria visible, shown in red. **(B)** In MS compared to controls, more axons contained mitochondria, and the **(C)** percentage of mitochondrial coverage of the axon was similar. **(D)** Reconstructed 3-D axons (SMI312 in green) and mitochondria (Tomm20 in red) of an MS donor. (**E**) In MS compared to controls, the

mitochondria frequency was higher (p=1.5e-4) and **(F)** the surface area of the mitochondria is similar.

Figure 6: Ultrastructural alterations are correlated to number of active and phagocytic microglia and number of T cells. Spearman correlation tests of ultrastructural alterations that were different in MS compared to controls and the number of activated microglia, phagocytic microglia and T cells. (**A**) The myelin density was negatively correlated to the number of $P2RY12^{-}HLA^{+}$ cells/mm^2 (p=0.001, r=-0.93), (**B**) the number of $Iba1^{+}CD68^{+}$ cells/mm^2 (p=0.007, r=-0.86) and (**C**) the number of $CD3^{+}$ T cells/mm^2 (p=0.047, r=-0.74). The axonal mitochondria frequency was positively correlated to (**D**) the number of $P2RY12^{-}HLA^{+}$ cells/mm^2 (p=0.015, r=0.81) and (**E**) the number of $Iba1^{+}CD68^{+}$ cells/mm^2 (p=0.047, r=0.71). The length of CASPR1 was positively correlated to (**F**) the number of $CD3^{+}$ T cells/mm^2 (p=0.021, r=0.79). The length of Kv1.2 was positively correlated to (**G**) the number of $P2RY12^{-}HLA^{+}$ cells/mm^2 (p=0.021, r=0.79) and (**H**) the number of $CD3^{+}$ T cells/mm^2 (p=0.015, r=0.81). The percentage overlap of CASPR1 with Kv1.2 was positively correlated to (**I**) the number of $P2RY12^{-}HLA^{+}$ cells/mm^2 (p=0.015, r=0.81), (**J**) the number of $Iba1^{+}CD68^{+}$ cells/mm^2 (p=0.002, r=0.91) and (**K**) the number of $CD3^{+}$ T cells/mm^2 (p=0.047, r=0.71).

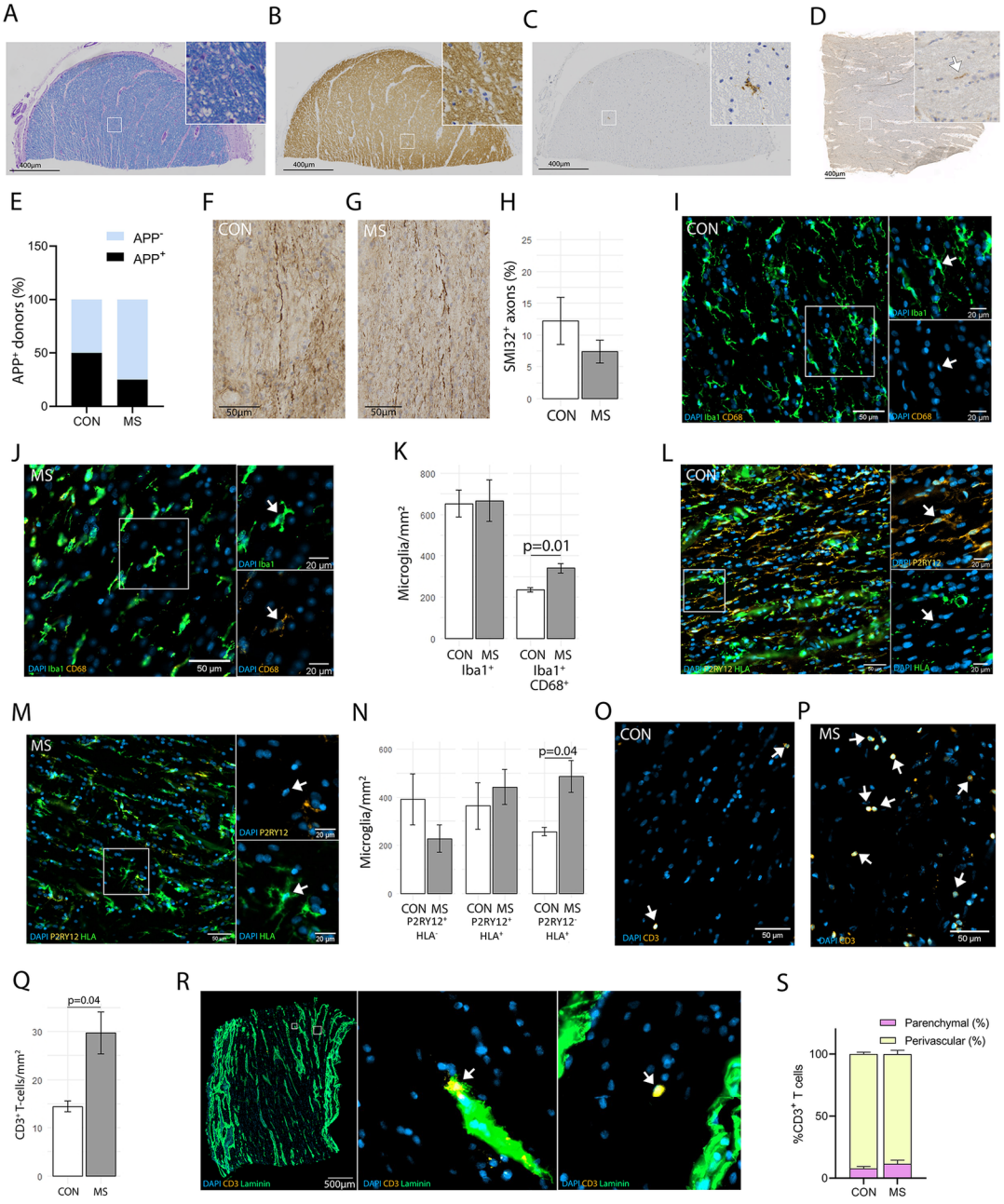

ANA_26585_Figure 1_Rebuttal2_trimmed2.tif

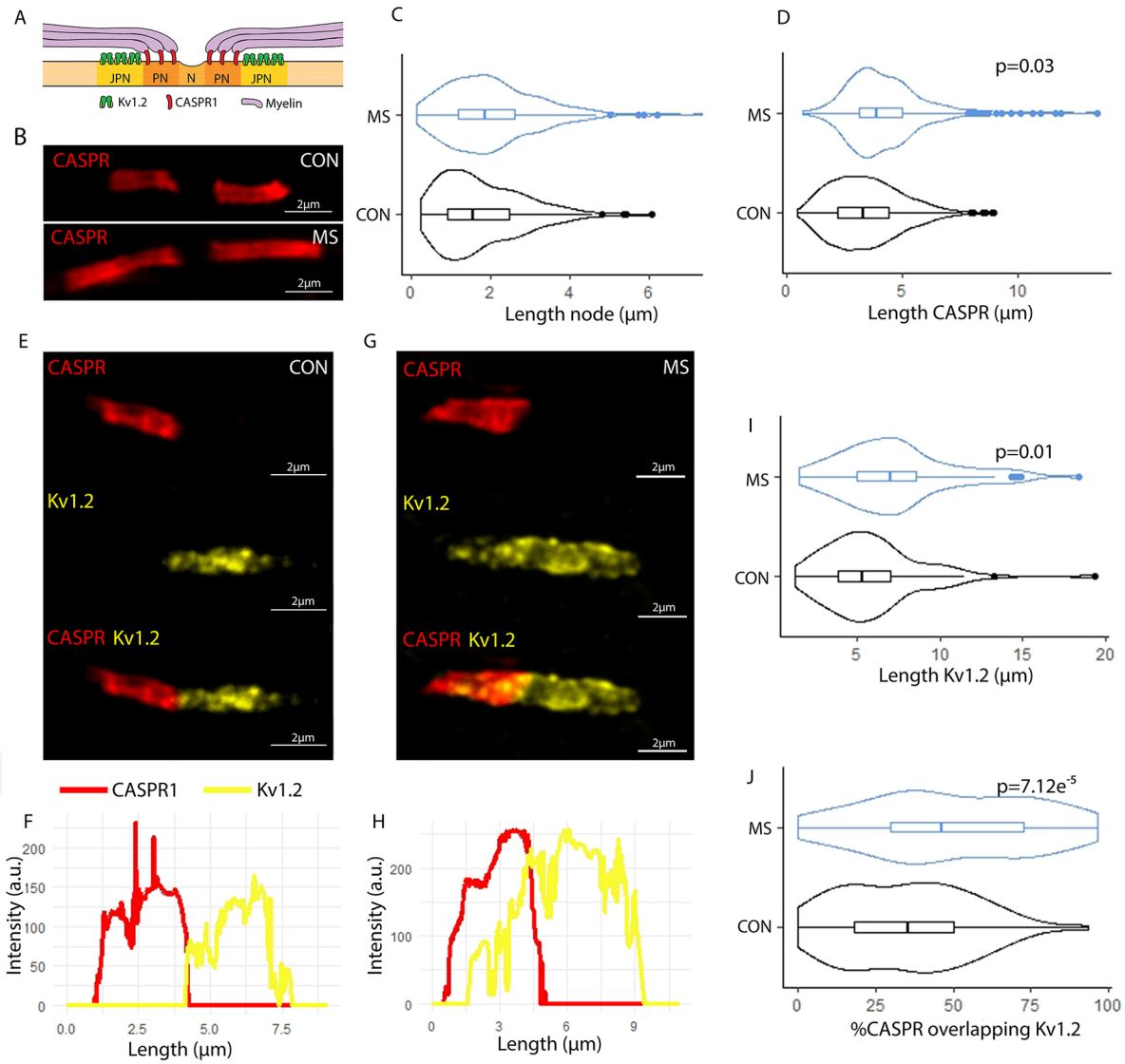

ANA_26585_Figure 2_Rebuttal2_trimmed.tif

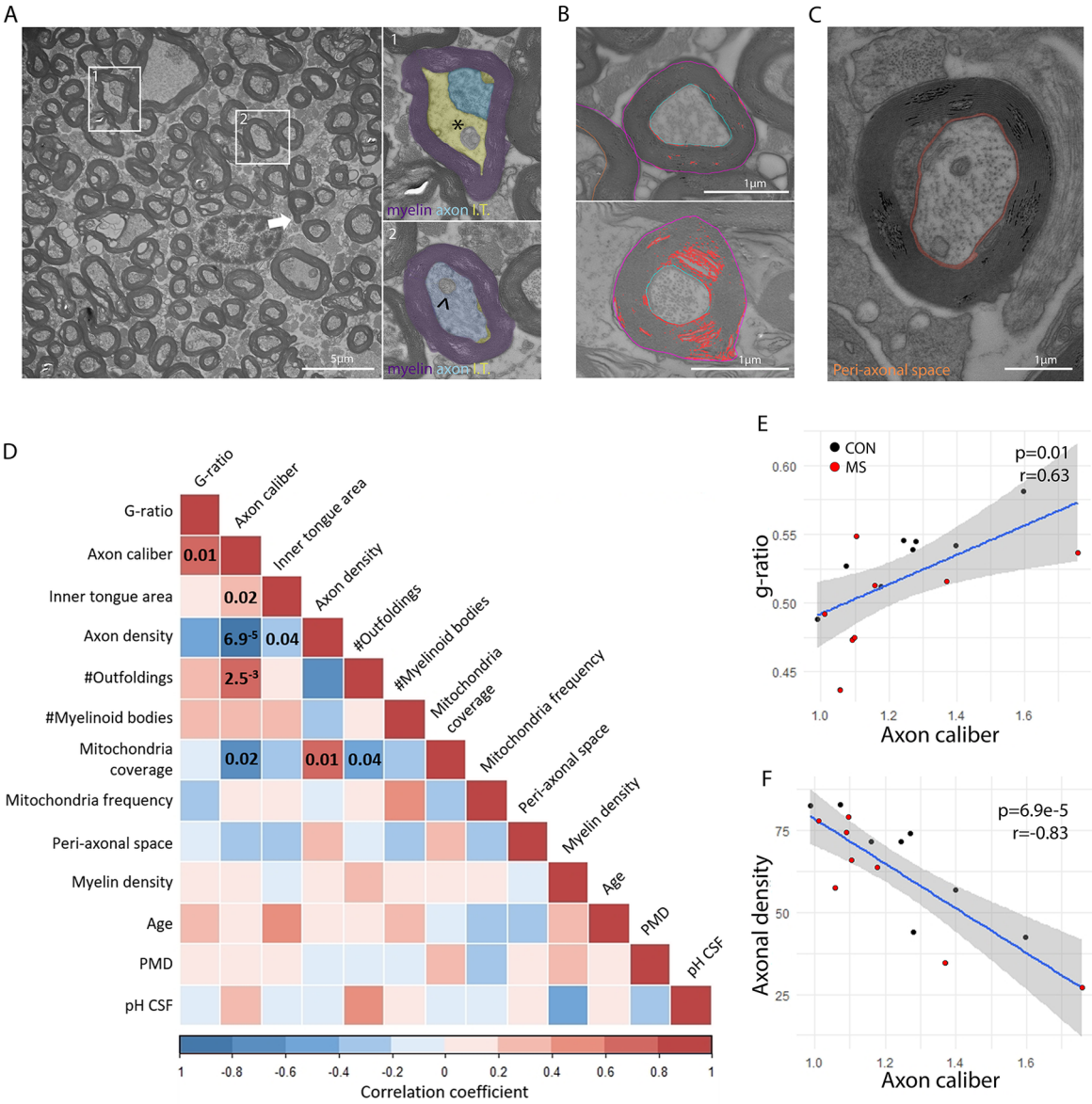

ANA_26585_Figure 3_Rebuttal2_trimmed.tif

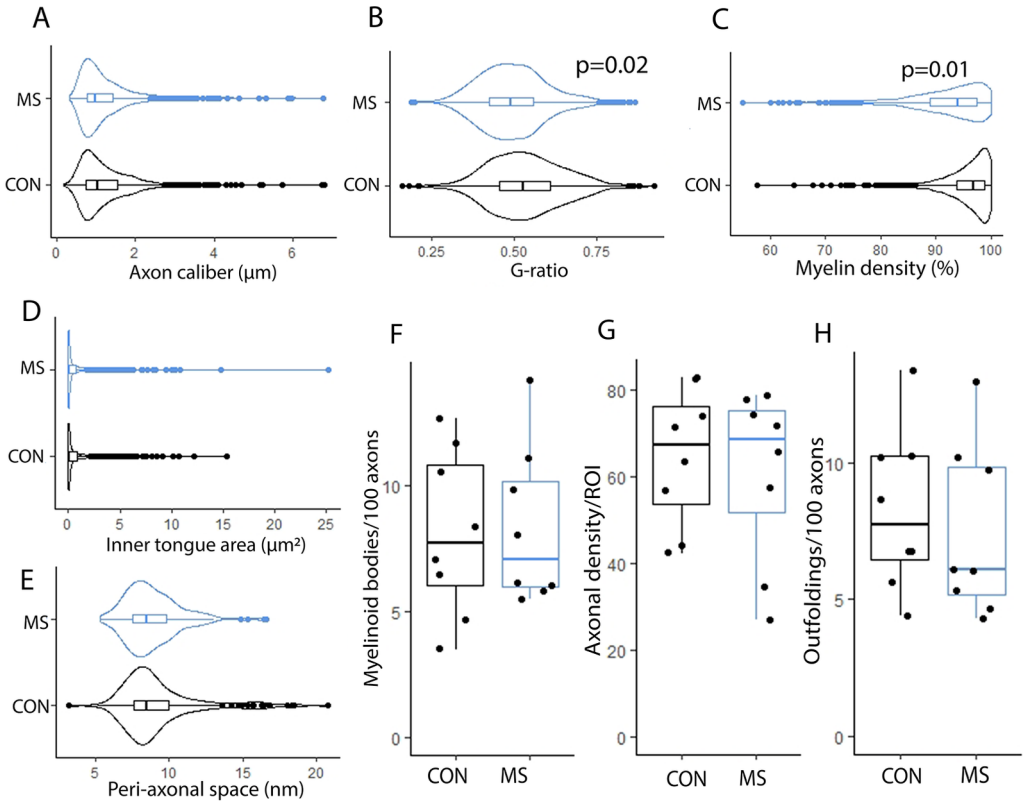

ANA_26585_Figure 4_Rebuttal2_trimmed.tif

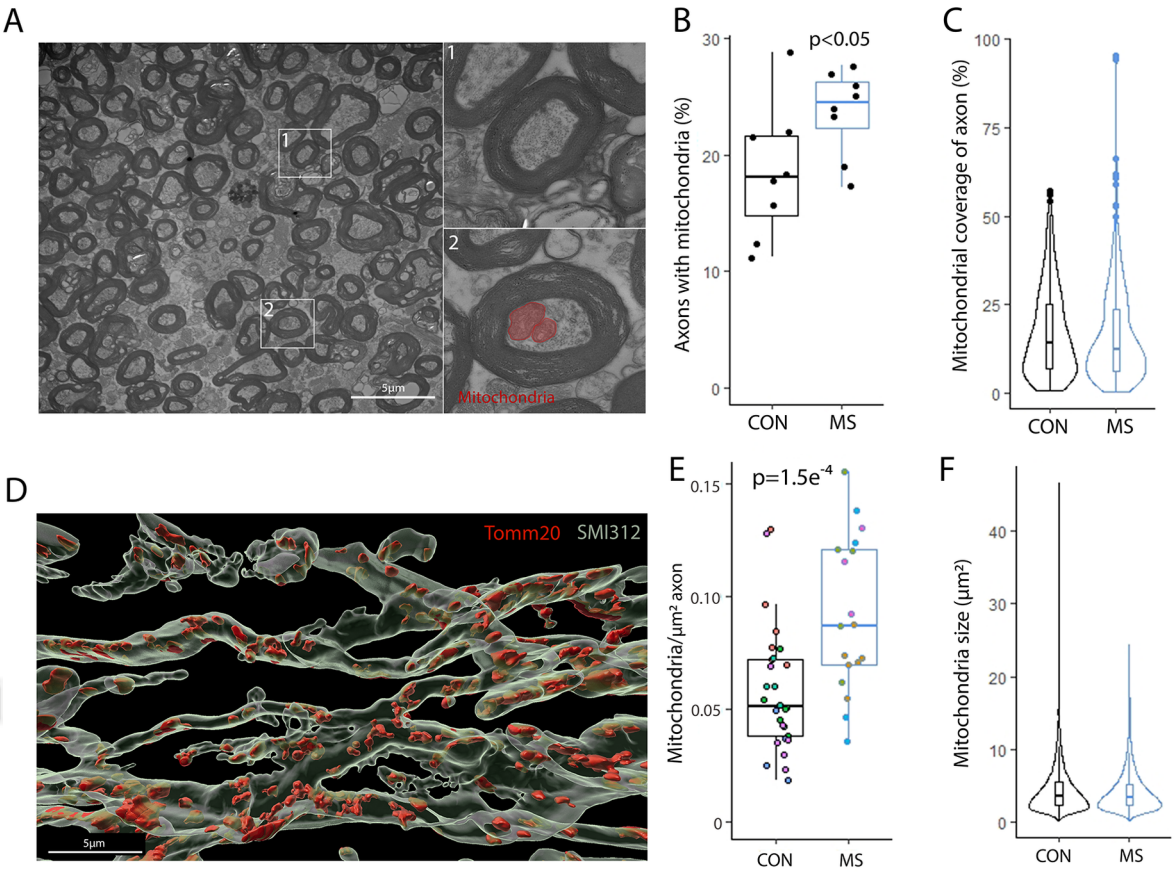

ANA_26585_Figure 5_Rebuttal2_trimmed.tif

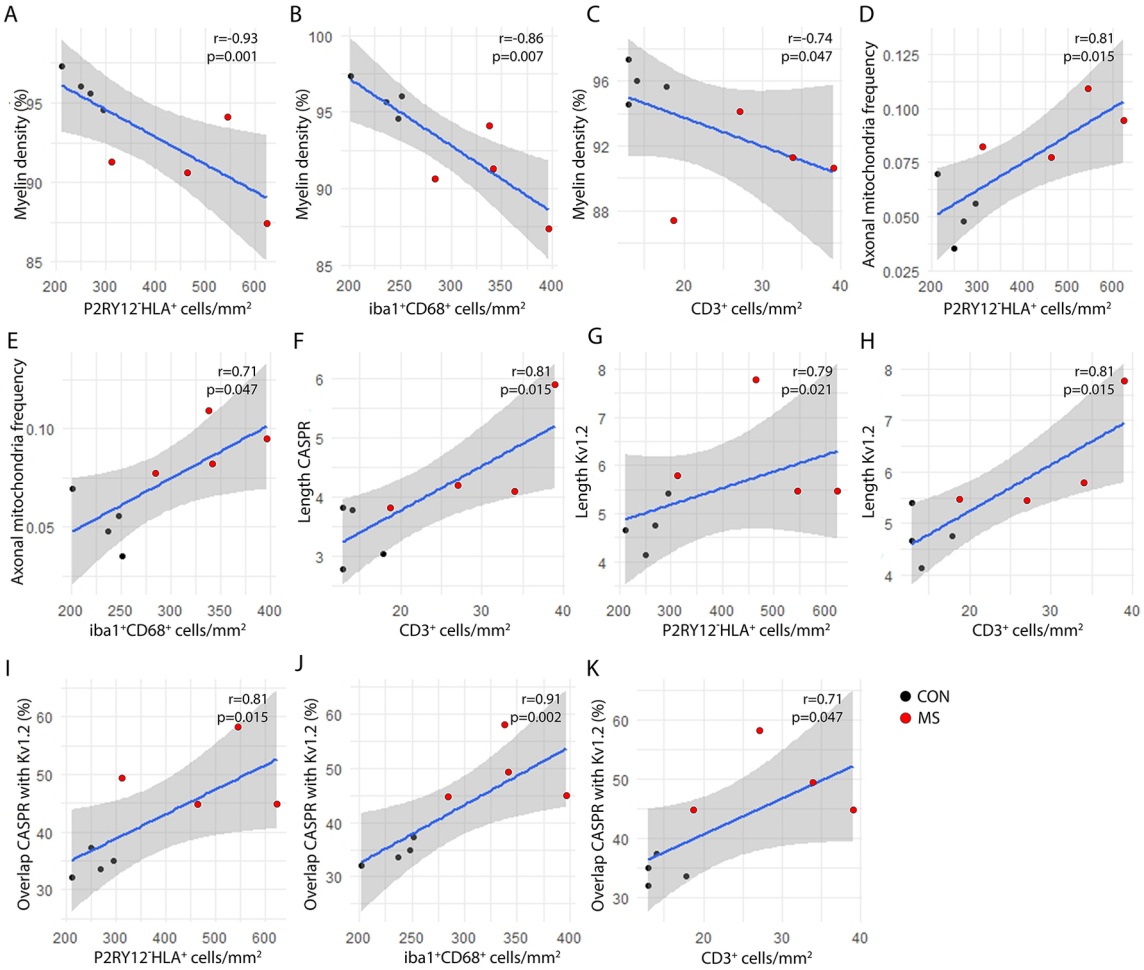

ANA_26585_Figure 6_rebuttal2_trimmed.tif

Table 1: Antibodies

Primary antibody	Company (Cat#)	Dilution	Antigen retrieval
HLA	DAKO (M077501-2)	Frozen: 1:500 FFPE: 1:100	Frozen: - FFPE: PBS, pH7.6, 10 min, 700 W
PLP	BioRad (MCA839G)	Frozen: 1:6,000 FFPE: 1:500	Frozen: - FFPE: PBS, pH7.6, 10 min, 700 W
Kim1P	Kindly gifted by Prof. Dr. Heinz-Joachim Radzun, Göttingen	1:5,000	Citrate buffer, pH6, 10 min, 700 W
APP	EMD Millipore (MAB348)	1:2,000	-
SMI32	Covance (LN# E11HF01669)	1:1,000	-
P2RY12	Kindly gifted by Dr. Chotima Böttcher, Charité Berlin	1:1,500	-
Iba1	Wako (019-19741)	1:750	-
CD68	DAKO (M0814)	1:750	-
CD3	DAKO (A0452)	1:100	Citrate buffer, pH6, 30 min, 80°C
CD3	Abcam (ab699)	1:50	-
Laminin	Sigma (L9393)	1:100	-
CASPR	Abcam (ab34151)	1:200	Citrate buffer, pH6, 3 hours, 60°C
Kv1.2	Alomone (APC-010)	1:100	Citrate buffer, pH6, 3 hours, 60°C
Tomm20	Abcam (ab186735)	1:200	Citrate buffer, pH6, 30 min, 80°C
CD19	Biolegend (115501)	1:100	Citrate buffer, pH6, 30 min, 80°C
CD138	BioRad (MCA2459T)	1:100	Citrate buffer, pH6, 30 min, 80°C
SMI312	Biolegend (837901)	1:750	Citrate buffer, pH6, 30 min, 80°C

Abbreviations: FFPE = formalin fixed paraffin embedded, PBS = phosphate buffered saline

Table 2: Donor demographics and characteristics of MS severity and pathology

	IHC			TEM		
	CON (n=4)	**MS (n=4)**	**p-value**	**CON (n=8)**	**MS (n=8)**	**p-value**
Age in years (SD)	87.50 (7.94)	72.25 (10.24)	n.s.	85.88 (6.38)	70.13 (7.22)	4.1e-4
Sex (F%)	100%	25%	0.03	100%	50%	0.02
PMD in hours (SD)	6:41 (1:50)	6:36 (1:37)	n.s.	7:12 (1:34)	6:59 (1:39)	n.s.
pH of CSF (SD)	6.57 (0.21)	6.60 (0.28)	n.s.	6.58 (0.19)	6.57 (0.26)	n.s.
Age at onset (SD)	-	39.25 (13.45)	-	-	37.38 (11.11)	-
DOD (SD)	-	33.25 (11.15)	-	-	32.88 (9.88)	-
Severity score (SD)	-	2.35 (1.56)	-	-	3.05 (1.28)	-

Abbreviations: CSF = cerebrospinal fluid, DOD = duration of disease, IHC = immunohistochemistry, PMD = post-mortem delay, SD = standard deviation, TEM = transmission electron microscopy. P-values calculated with unpaired two-sided T-test.

Aletta Marthe Roswitha van den Bosch

alettavdb@hotmail.com